Functionalization of SBA-15 with CeO 2 nanoparticles for adsorptive desulfurization: Matters of template P123

5 authors, including:

Yu Yin
Jiangsu University of Science and Technology
14 PUBLICATIONS   **291** CITATIONS

Functionalization of SBA-15 with CeO$_2$ nanoparticles for adsorptive desulfurization: Matters of template P123

Yu Yin and Zhi-Hao Wen
Jiangsu University of Science and Technology, P. R. China

Xiao-Qin Liu
Nanjing Tech University, P. R. China

Ai-Hua Yuan
Jiangsu University of Science and Technology, P. R. China

Lei Shi
Chinese Academy of Sciences, P. R. China

Abstract
Adsorption is one of the most promising methods for desulfurization of transportation fuels, due to the strategy which enables removal of organic sulfur compounds to be conducted at ambient conditions with high efficiency. Adsorbent is the key to the adsorptive performance. Both π complexation and direct sulfur metal bonds are efficient methods for adsorptive desulfurization. For construction of these bonds, it is necessary to introduce active metal species on the support. In this work, Ce(NO$_3$)$_2$ was directly introduced into the as-synthesized SBA-15, and high dispersion of CeO$_2$ nanoparticles was obtained. With the loading content of 12–46 wt%, the particle sizes of the CeO$_2$ NPs are in the range of 4.4–6.3 nm. The good dispersion status of CeO$_2$ nanoparticles is contributed to the template P123 preserved in as-synthesized SBA-15, which provides a confined space for the dispersion of CeO$_2$ nanoparticles. However, the large CeO$_2$ particles (7.0 nm) are formed for the sample originated from template-free SBA-15. We also demonstrate that the adsorptive performance of SBA-15 is enhanced with the modification of CeO$_2$ nanoparticles. Besides, the performances of CeO$_2$ nanoparticle-modified samples stay in step with the dispersion status of the CeO$_2$ nanoparticles.

Keywords
CeO$_2$ nanoparticles, mesoporous silica, desulfurization, confined space, adsorption

Corresponding author:
Yu Yin, Jiangsu University of Science and Technology, 2 Mengxi Road, Jingkou District, Zhenjiang, Jiangsu 212003, China.
Email: season_july@just.edu.cn

Introduction

Deep desulfurization from transportation fuels has been of great urgency due to more stringent environmental regulations worldwide (Cao et al., 2008; Sitamraju et al., 2015; Wang et al., 2012). Besides, fuel cell technologies call for the hydrogen resource with nearly zero sulfur content (Kannan and Kumar, 2016; Speder et al., 2016). Nowadays, refineries mainly rely on the hydro-desulfurization (HDS) process to remove sulfur compounds in industry. HDS technology is operated at harsh conditions, including super-high temperatures of 300–350°C and ultrahigh hydrogen pressures of 2–10 MPa (Shang et al., 2004; Singh and Kunzru, 2016; Sun and Prins, 2008; Vit et al., 2015). The HDS technology is efficient in removing inorganic sulfur compounds, including thiols and sulfides. However, it is less effective to remove organic sulfur compounds, including thiophene and its derivatives (Dai et al., 2006; Yang et al., 2003). It is highly desirable to further decline the sulfur concentration. Removal of organic sulfur compounds has been researched by various methods, including extraction, oxidation, and biological strategy (Moghadam et al., 2017; Xu et al., 2017). It is fortunate that these methods show positive effects on the removal of organic sulfur compounds. However, they inevitably show some shortcomings referring to consuming energy, producing byproducts, and generating slow biodegradation. There is thereby an urgent need but it is still a significant challenge to achieve deep desulfurization levels. Among the alternatives, one of the most important future directions of desulfurization is adsorption. There is great potential in using adsorbents for deep desulfurization, because organic sulfur molecules can be captured at ambient conditions with high efficiency (Song et al., 2014; Vilarrasa-Garcia et al., 2011b; Xiong et al., 2010). It is commonly known that both π complexation and direct sulfur metal (S–M) bonds can work for adsorptive desulfurization (Danmaliki and Saleh, 2017; Khan et al., 2017; Shi et al., 2017 Song et al., 2013). Thus, active species, such as Cu_2O (Jiang et al., 2013; Wang et al., 2009b), CeO_2 (Song et al., 2016; Xiao et al., 2013a), etc. are always incorporated into the porous materials for fabrication of π complexation or direct S–M sites. It is known that the porous materials with high surface areas are highly desirable for loading active species (Li et al., 2016; Xiao et al., 2013b; Yin et al., 2016). In addition, it is demonstrated in a number of studies that key to the adsorption performance of the adsorbent is the status of supported active species (Hernández-Maldonado and Yang, 2004b; Song et al., 2011).

Since the M41-typed mesoporous materials were first synthesized in 1992, a large number of mesoporous materials have been synthesized by use of the surfactant template method (Feng et al., 2012; Liu et al., 2002; Stein, 2003; Thomas, 2010). Among the mesoporous materials, mesoporous silica shows high surface areas and modest pore sizes and is very suitable for application as the support (Cruz et al., 2016; Eedugurala et al., 2015; Gaudin et al., 2016; Sun et al., 2015; Zhang et al., 2008). In general, mesoporous silica is a promising host for preparation of the selective adsorbent (Anbia and Mohammadi, 2008; Tian et al., 2010; Wang et al., 2006; Yin et al., 2014). Normally, the as-synthesized mesoporous silica is first to calcine, which leads to generate template-free mesoporous silica with open pores. The precursor is then incorporated into the open pores, with the second calcination to convert the precursor to active species (Cheng et al., 2015; Shao et al., 2012; Vilarrasa-Garcia et al.,

2011b). This conventional method requires repeated calcination, which is low efficiency and energy consuming. According to the previous reports of Zhu and Liu's groups, there is a special confined space between template P123 and silica walls in as-synthesized mesoporous silica (Yin et al., 2012; Yue et al., 2008). By direct introduction of the precursor into the as-synthesized SBA-15 (ASS), high dispersion of active species is achieved by use of the extraordinary confined space.

Herein, we report for a new strategy for functionalization of mesoporous silica SBA-15 with CeO_2 nanoparticles (NPs) in order to prepare adsorbents for desulfurization. Before removal of the template P123, $Ce(NO_3)_2$ was directly introduced into ASS via solid-state grinding. Followed with calcination in air, the resultant adsorbents were obtained. We denoted the adsorbents as CeO_2-ASS. For contrast, $Ce(NO_3)_2$ was introduced into template-free SBA-15 (TFS) as well for preparation of the CeO_2-TFS sample. The results show that by use of ASS as the support, the CeO_2 NPs are controlled in the size of 4.4–6.3 nm. The confined space between template P123 and silica walls in ASS plays an important role on the high dispersion of CeO_2 NPs. For the sample based on TFS, however, the large CeO_2 NPs (7.0 nm) are formed and give rise to partly disordered and blocked pores of SBA-15. We also demonstrate that the CeO_2 NP-modified materials show better performances than pure SBA-15 on adsorptive desulfurization. This is contributed to the formation of S–M bonds between CeO_2 and thiophene. It is important to highlight that the CeO_2-ASS samples show much better adsorptive desulfurization performances than CeO_2-TFS.

Experimental

Materials synthesis

ASS and TFS. Mesoporous silica SBA-15 was synthesized following the literature method, which was first reported by Zhao et al. (1998). Two gram of pluronic $EO_{20}PO_{70}EO_{20}$ (P123) was first added to 75 g of HCl aqueous solution (1.6 m). The mixture was stirred for half an hour. After dissolving, 4.25 g of silica source tetraethylorthosilicate was added. Then, stirring was conducted once again at 40°C for 24 h. The mixture was then transferred to the teflon-lined autoclave for hydrothermal treatment at 100°C for 24 h. After cooling to room temperature, the powder was collected by filtration. ASS was obtained after the powder was dried at room temperature. TFS was obtained by removal of template P123, which was conducted by calcination at 550°C for 5 h in flowing air.

xCeO₂-ASS. The precursor $Ce(NO_3)_3 \cdot 6H_2O$ was introduced into ASS via solid-state grinding at room temperature for 30 min. The thoroughly mixed powder was calcined in flowing air at 500°C for 5 h to form active CeO_2 NPs, and template P123 was removed simultaneously. The obtained composites were denoted as $xCeO_2$-ASS, where x represents the weight ratio of CeO_2 in the CeO_2-ASS samples.

xCeO₂-TFS. In a conventional process, $xCeO_2$-TFS samples were prepared by introduction of $Ce(NO_3)_3 \cdot 6H_2O$ into TFS via solid-state grinding at room temperature for 30 min. The thoroughly mixed powder was calcined in flowing air at 500°C for 5 h to form active CeO_2 NPs. The obtained composites were denoted as $xCeO_2$-TFS, where x represents the weight ratio of CeO_2 in the CeO_2-TFS samples.

Characterization

XRD spectra were collected with a Bruker D8 Advance diffractometer using Cu $K\alpha$ radiation in the 2θ ranges from $0.7°$ to $6°$ (for low-angle patterns) and $5°$ to $70°$ (for wide-angle patterns) at $40\,kV$ and $40\,mA$. High-resolution transmission electron microscopy (HRTEM) was performed on a Tecnai G2 F30 S-Twin electron microscope operated at $300\,kV$. The N_2 isotherms were measured using a BELSorp-max system at $77\,K$. Prior to measurement, the samples were pretreated under vacuum at $200°C$ for $4\,h$. The Brunauer–Emmett–Teller surface areas were calculated according to the adsorption branch in the relative pressure of 0.04–0.20. The total pore volumes were evaluated at the relative pressure of 0.99. The pore size distributions were calculated by Barrett–Joyner–Halenda method according to the desorption branch. The ceria content of a sample was tested on J-A1100 inductively coupled plasma-optical emission spectrometry.

Fourier transform infrared (IR) spectra were recorded on a Nicolet Nexus 470 spectrometer with a spectral resolution of $2\,cm^{-1}$ using transparent KBr pellets. Thermogravimetric (TG) analysis was performed on a thermobalance (STA-499C, NETZSCH). About $10\,mg$ of sample was heated from the room temperature to $800°C$ in a flow of air ($25\,ml\,min^{-1}$).

Adsorptive test

The simulated fuel was prepared using thiophene as the representative of organic sulfur contaminants. By mixing thiophene with isooctane, the sulfur concentration was controlled to be $550\,ppmw$ (parts per million by weight). The desulfurization performance of adsorbents was evaluated on the basis of breakthrough curves. Experiments were performed at room temperature in a vertical quartz column with $6\,mm$ in diameter. Adsorbents ($0.2\,g$) were filled into the vertical quartz column, and a quartz grid was supported. Prior to measurement, the adsorbents were activated in situ by calcination at $200°C$ for $2\,h$ in air. After cooling to room temperature, the gas of air was switched to the simulated fuel, which was pumped up with a mini creep pump at a rate of $3.0\,ml\,h^{-1}$. Effluent solutions were collected at regular intervals until saturation was reached. The sulfur content in effluent solutions was determined with a Varian 3800 gas chromatograph (GC) equipped with a pulsed-flame photometric detector. A calibration curve was prepared to analyze the GC results. Breakthrough curves were generated by plotting the normalized sulfur concentration versus the cumulative fuel volume. The normalized concentration (c/c_0) was obtained from the detected content (c) divided by the initial content (c_0), and the cumulative fuel volume was normalized by the adsorbent weight. The adsorption capacity was calculated by integral calculus.

Results and discussion

Status of supported CeO$_2$ NPs

Figure 1(a) depicts the low-angle XRD patterns of SBA-15, CeO$_2$-ASS, and CeO$_2$-TFS samples. Mesoporous silica SBA-15 shows an intense diffraction line indexed as (100), and two weak lines indexed as (110) and (200) reflections. This indicates that SBA-15 contains a 2D *p6mm* hexagonal symmetry. All of the ceria-containing samples show the similar patterns with SBA-15. This indicates the ordered mesoporous structures are well maintained after the
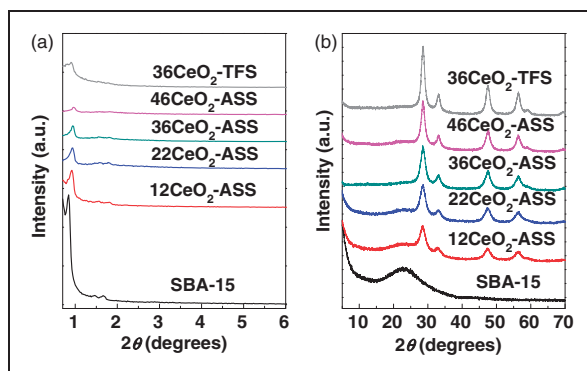
Figure 1. (a) Low-angle and (b) wide-angle XRD patterns of SBA-15, CeO_2-ASS, and CeO_2-TFS samples. ASS: as-synthesized SBA-15; TFS: template-free SBA-15; XRD: X-ray diffraction.

Table 1. Physicochemical properties of SBA-15, CeO_2-ASS, and CeO_2-TFS samples.

| Sample	CeO_2 content[a] (wt%)	S_{BET} ($m^2 g^{-1}$)	V_p ($cm^3 g^{-1}$)	D_p (nm)		d_{CeO2}[b] (nm)	Adsorption capacity at saturation (mmol S g^{-1})
SBA-15	0	875	1.137	5.9	–	–	0.105
12CeO$_2$-ASS	12.3	830	1.049	6.3	3.6	4.4	0.131
22CeO$_2$-ASS	22.1	754	0.900	6.3	3.6	4.6	0.159
36CeO$_2$-ASS	36.2	573	0.711	6.3	3.6	5.1	0.165
46CeO$_2$-ASS	46.3	432	0.495	3.6	5.9	6.3	0.136
36CeO$_2$-TFS	36.3	484	0.579	3.7	–	7.0	0.115

ASS: as-synthesized SBA-15; BET: Brunauer–Emmett–Teller; TFS: template-free SBA-15.
[a]ICP data.
[b]CeO_2 crystallite size calculated by the Scherrer formula.

introduction of CeO_2. In addition, in comparison with SBA-15, the intensity of the (100) reflection of CeO_2-ASS and CeO_2-TFS samples declines. The weak intensity of diffraction peaks results from the decreased scatter contrast between silica walls and pore space, which is presumably due to the incorporation of CeO_2 into pores of SBA-15.

The wide-angle XRD patterns of the samples are shown in Figure 1(b). From the patterns of support SBA-15, a broad diffraction peak can be seen at 2θ of 23°, which is attributed to amorphous silica. For the samples of CeO_2-ASS and CeO_2-TFS, some new peaks at 2θ of 28.5°, 33.2°, 47.5°, and 56.3° derived from CeO_2 (JCPDS 81-0792) emerge on the pattern. This indicates that the CeO_2 species do exist in the samples. Besides, for the CeO_2-ASS samples, the CeO_2 peaks become intense with the increase of ceria content. It should be noted that the diffraction peaks of CeO_2 for the 36CeO$_2$-TFS sample are more intense than all of the CeO_2-ASS samples. The average particle sizes of CeO_2 NPs in the samples were calculated by the Scherrer formula based on full width at half maximum values from CeO_2 peaks at 2θ of 28.5°. Table 1 displays the results of particle sizes. The particle sizes of CeO_2 NPs in the CeO_2-ASS samples are in the range of 4.4–6.3 nm. While the CeO_2 NPs in the
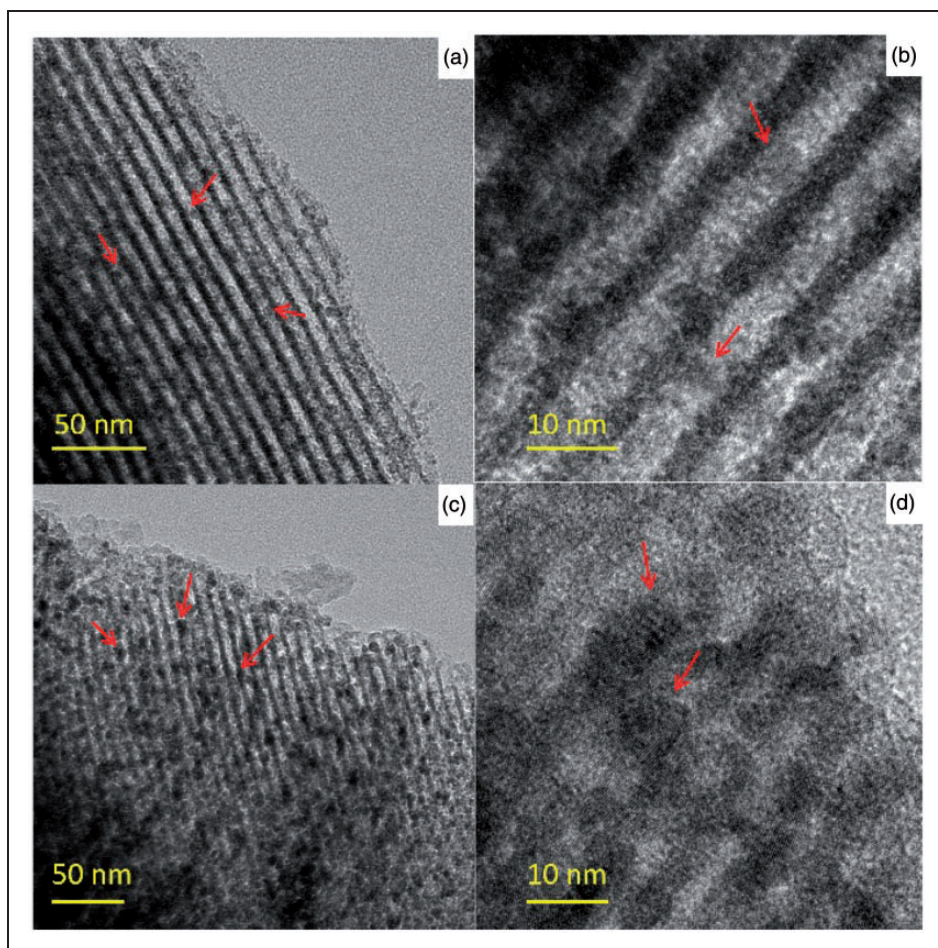
Figure 2. HRTEM images of (a), (b) for 36CeO$_2$-ASS and (c), (d) for 36CeO$_2$-TFS samples.
ASS: as-synthesized SBA-15; HRTEM: high-resolution transmission electron microscopy; TFS: template-free
SBA-15.

36CeO$_2$-TFS sample show the particle size of 7.0 nm, which is remarkably larger than the
36CeO$_2$-ASS sample (5.1 nm).

Figure 2 shows the HRTEM images of CeO$_2$-ASS and CeO$_2$-TFS samples. The TEM
image of pure SBA-15 is presented in Figure S1. The silica walls of SBA-15 appear as dark,
and pore spaces appear as white. Thus, highly ordered pore structures of SBA-15 can be
judged. After functionalization of SBA-15 with ceria, the TEM images have a slight change.
For the 36CeO$_2$-ASS sample, the mesopores keep with a long-range order as well as SBA-15.
In addition, some shadow areas appeared, which contributed to dispersed CeO$_2$ NPs on the
SBA-15. As for the 36CeO$_2$-TFS sample, CeO$_2$ NPs with large sizes can be identified.
Moreover, the channels of SBA-15 are found to be partly disordered and blocked by the
CeO$_2$ NPs.
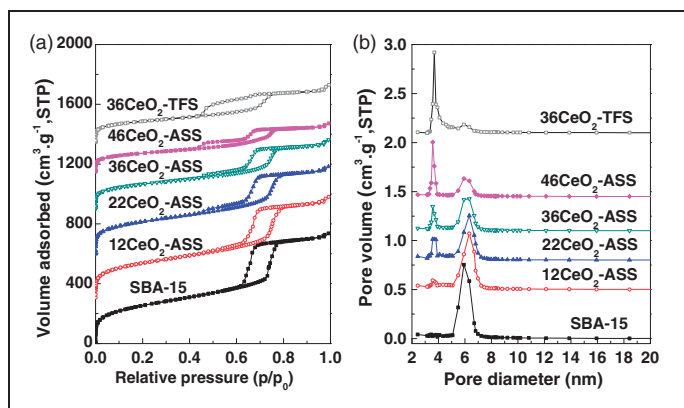
Figure 3. (a) N_2 adsorption–desorption isotherms and (b) pore size distributions of SBA-15, CeO_2-ASS, and CeO_2-TFS samples. Curves are plotted offset for clarity.
ASS: as-synthesized SBA-15; TFS: template-free SBA-15.

Figure 3(a) depicts the N_2 isotherms of the adsorbents. Figure 3(b) shows the pore size distribution curves calculated from the desorption branches of isotherms. Table 1 displays the surface areas, pore volumes, and pore sizes of the adsorbents. Support SBA-15 shows a type IV isotherm shape with an H1 hysteresis loop at the relative pressure (p/p_0) of 0.60–0.80. This is characteristic of materials with regular and cylindrical mesopores. In general, the isotherm shapes of $12CeO_2$-ASS, $22CeO_2$-ASS, and $36CeO_2$-ASS samples show great similarity to that of support SBA-15. There is difference on no more than closing point. For the $12CeO_2$-ASS, $22CeO_2$-ASS, and $32CeO_2$-ASS samples, the closing point of the hysteresis loop shifts to a slightly lower relative pressure of 0.45. This gives direct evidence of the introduction of oxides into the pores of SBA-15. For the $46CeO_2$-ASS sample, the closing point of the hysteresis loop is at the relative pressure of 0.45 as well. In addition, the desorption branch of the isotherm shows a serious delay, which gives rise to the two steps of desorption curves. This indicates that massive pore spaces should be occupied with the introduced oxides. The $36CeO_2$-TFS sample, derived from TFS, shows a great different isotherm curve with others. The hysteresis loop is parallel and horizontal at the relative pressure (p/p_0) of 0.40–0.75. This indicates that the sample contains slit pores. This result coincides with the partly disordered and blocked pores observed from the TEM image. When it comes to surface areas, SBA-15 shows the highest value of $875\,m^2\,g^{-1}$. The surface areas of the CeO_2-ASS samples are in the range of 830–$432\,m^2\,g^{-1}$. It is noteworthy that the $36CeO_2$-TFS sample shows the lower surface area and pore volume than $36CeO_2$-ASS, even if ceria content is identical. Further results show that the pore size of SBA-15 is 5.9 nm. For the $12CeO_2$-ASS, $22CeO_2$-ASS, and $36CeO_2$-ASS samples, the pore sizes are 6.3 nm in chief and 3.6 nm in minor. For the $46CeO_2$-ASS sample, the pore size is 3.6 nm in chief and 5.9 nm in minor. For the $36CeO_2$-TFS sample, the pore size is centered at 3.7 nm.

According to the XRD, TEM, and N_2 adsorption–desorption results, it is necessary to have a summary on the combination status of CeO_2 NPs and SBA-15. First, due to the similar low-angle XRD patterns with SBA-15, white dark contrast on the TEM images, and distinct hysteresis loop on the N_2 adsorption–desorption isotherms, it is safe to deduce that the mesoporous structures of SBA-15 are well preserved after the modification of CeO_2 NPs.

Second, on the basis of weaken intensity of (100) reflection on the low-angle XRD patterns, identified CeO_2 NPs on the TEM images, and movement of the closing point of the hysteresis loop on the N_2 adsorption–desorption isotherms, it is reasonable to believe that the CeO_2 NPs are introduced into the pores of SBA-15. Third, the CeO_2 NPs show various statuses with the diverse ceria content and synthetic methods. In detail, the sizes of CeO_2 NPs in the CeO_2-ASS samples derived from wide-angle XRD pattern are in the range of 4.4–6.3 nm. In comparison with $36CeO_2$-ASS (5.1 nm), the size of the CeO_2 NPs in the $36CeO_2$-TFS sample is larger (7.0 nm). Moreover, the $36CeO_2$-ASS sample shows higher surface area, pore volume, and pore size than the $36CeO_2$-TFS sample. These data are consistent with the notion that CeO_2 NPs in the CeO_2-ASS samples have better dispersion status than in CeO_2-TFS. In other words, the application of ASS as support is propitious to the high dispersion of CeO_2 NPs.

To further verify the location of the ceria, XPS analyses were carried out to study the surface properties of the samples. Figure S2 shows the results, and Table S1 summarizes the atomic concentration of Si, O, and Ce elements in the $36CeO_2$-ASS and $36CeO_2$-TFS samples. The theoretical value of the atomic concentration of Ce is 30.78. It is unusual that the value measured with XPS technique (1.03, 1.12) is much lower than the theoretical value (30.78). Take in mind that the XPS is the surface technique. The measured low atomic concentration of Ce is due to the formation of aggregated ceria on the surface of SBA-15. What needs to be emphasized is that the concentration is strongly low both in the $36CeO_2$-ASS and $36CeO_2$-TFS samples. Thus, it is safe to say that the location of most ceria is inside the mesopores of the porous silica rather than on the surface.

## Proposed mechanism for high CeO_2 dispersion in CeO_2-ASS

IR spectra of the samples before and after calcination are presented in Figure 4. The bands in the range of 2850–3000 and 1350–1500 cm^{-1} appearing on the spectrum of ASS are the
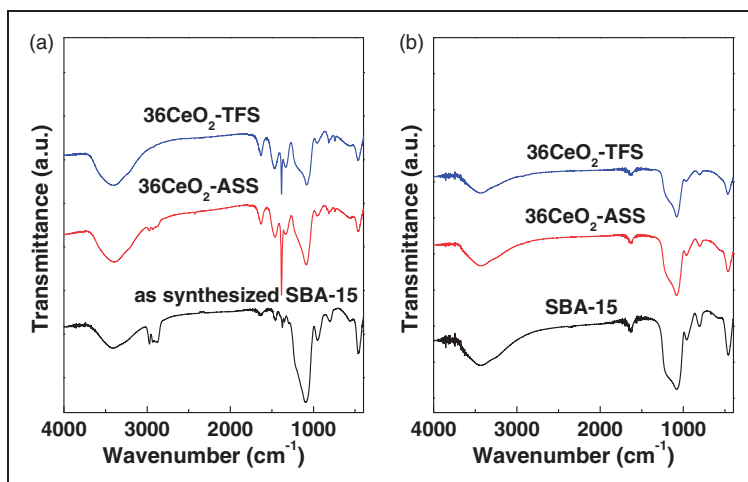
Figure 4. IR spectra of SBA-15, CeO_2-ASS, and CeO_2-TFS samples (a) before and (b) after calcination. ASS: as-synthesized SBA-15; TFS: template-free SBA-15.

characteristics of template P123 (Figure 4(a)) (Tian et al., 2002). With calcination, ASS transforms to TFS, the bands of template P123 is absent, which is ascribed to massive decomposition of the template P123. The carbon content in ASS is 30.59 wt%, after calcination, the carbon content in SBA-15 goes down to 0.32 wt%. This indicates that there is little carbonaceous substance remaining after the removal of template P123. With introduction of $Ce(NO_3)_2$ into ASS, some new bands at $1380\,cm^{-1}$ appeared in the $36CeO_2$-ASS sample. The new bands are due to the asymmetric stretching vibration of N–O (Yin et al., 2012), which illustrates the existence of NO_3^-. For the $36CeO_2$-ASS sample after calcination, the bands belonging to both template P123 and NO_3^- are invisible. This indicates that both template removal and $Ce(NO_3)_2$ conversion can finish in a step of calcination. The conversion of $Ce(NO_3)_2$ in the CeO_2-TFS sample is also conscious by comparing the spectra before and after calcination.

As shown in Figure 5, the decomposition behaviors of the samples are investigated by the TG technique. In ASS, the removal of template P123 takes place from 155 to 270°C with a massive weight loss of 50%. In cooperation, there is a sharp DTG peak at 162°C. It is worthwhile to note that pure P123 decomposes at about 210°C (Zhao et al., 1998). In comparison, the decomposition temperature of P123 in ASS is lower than pure P123. There is the strong possibility that the silica frameworks in ASS catalyze the removal of the template P123. For the $Ce(NO_3)_2$-modified template-free SBA-15 sample ($36CeO_2$-TFS), the decomposition procedure due to evaporation of adsorbed water goes from room temperature to 80°C. The decomposition of $Ce(NO_3)_2$ in $36CeO_2$-TFS proceeds from 80 to 450°C with a weight loss of 35.5%, which coincides with the calculated value of 35.7%. This indicates the massive conversion of $Ce(NO_3)_2$ to CeO_2. For the $Ce(NO_3)_2$-modified ASS, the curve of weight loss shows its own characteristics. In the $36CeO_2$-ASS sample, the conversion of $Ce(NO_3)_2$ in ASS starts from 80 to 168°C. There is a weight loss of 25.2%, which is well consistent with the calculated value of 25.3%. This suggests the massive conversion of $Ce(NO_3)_2$ to CeO_2 as well. Subsequently, the removal of template P123 starts from 168 to 355°C, corresponding to a sharp DTG peak at 208°C.
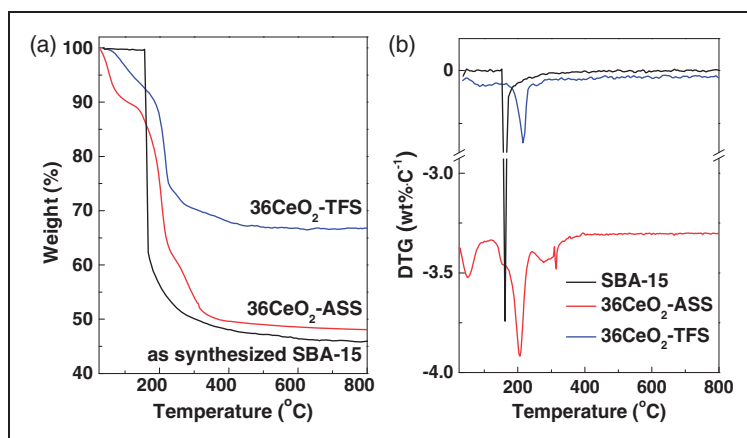

Figure 5. (a) TG and (b) DTG curves of SBA-15, CeO_2-ASS, and CeO_2-TFS samples before calcination. DTG curves are plotted offset for clarity.
ASS: as-synthesized SBA-15; DTG: derivative thermogravimetric; TFS: template-free SBA-15; TG: thermogravimetric.

According to the aforementioned results, CeO_2 NPs in the CeO_2-ASS samples show better dispersion status than in CeO_2-TFS. Next, we explored the proposed reasons. For the CeO_2-ASS samples, $Ce(NO_3)_2$ was directly introduced into the ASS with template P123. IR results prove that both template removal and $Ce(NO_3)_2$ conversion can be achieved in a step of calcination. TG results show that the removal of P123 in $36CeO_2$-ASS occurs at temperature of $216°C$. This decomposition temperature is much higher than that in ASS ($162°C$) and almost the same as pure P123 ($210°C$). This word points that the $Ce(NO_3)_2$ is indeed incorporated into the confined space between template P123 and silica walls. Therefore, the catalysis of silica walls to the decomposition of the template P123 does not work. We have noticed that the conversion of $Ce(NO_3)_2$ in the $36CeO_2$-ASS sample completes before the decomposition of template P123. That is to say, the conversion of $Ce(NO_3)_2$ is carried through within the confined space. Hence, at current time, we have to demonstrate that the conversion order of precursor and template P123 is key to the dispersion status of CeO_2 NPs. If the conversion of precursor takes precedence over the removal of template P123, the confined space will give a boost for the high dispersion of CeO_2 NPs. Otherwise, the earlier decomposition of template P123 will result in the damage of the confined space. As for the $36CeO_2$-TFS sample, the template P123 decomposes before the introduction of $Ce(NO_3)_2$. Therefore, the template P123 can no longer play a role on the dispersion status of CeO_2 NPs. To this end, we show that the better CeO_2 dispersion in CeO_2-ASS results from the confined space in ASS.

Performance on adsorptive desulfurization

The adsorptive desulfurization performances of the samples are measured with the simulated fuels, which contain 550 ppmw of sulfur. The breakthrough curves are shown in Figure 6. The values of adsorption capacity were calculated according to the breakthrough curves at saturation, and results are listed in Table 1. The support SBA-15 is capable of $0.105 \, \text{mmol g}^{-1}$ of thiophene, which exhibits the worst performance among all the samples. After modification of SBA-15 with CeO_2 NPs, the desulfurization capacities evidently
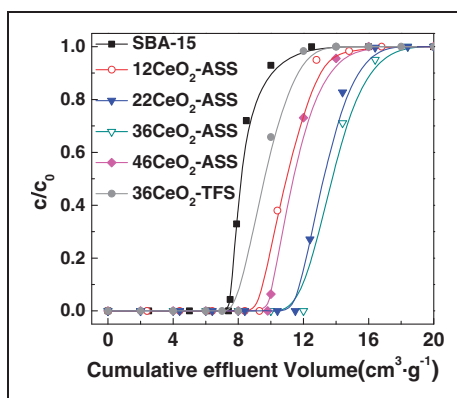
Figure 6. Breakthrough curves of thiophene in a fixed-bed adsorber with SBA-15, CeO_2-ASS, and CeO_2-TFS samples.
ASS: as-synthesized SBA-15; TFS: template-free SBA-15.

improve. The adsorption capacities for the $12CeO_2$-ASS, $22CeO_2$-ASS, and $36CeO_2$-ASS samples step up from 0.131 to 0.165 mmol g^{-1} with the increase of ceria content. For the sample of $46CeO_2$-ASS, the adsorption capacity is 0.136 mmol g^{-1}. The counterpart sample of $36CeO_2$-TFS shows the worst performance among all the CeO_2 NP-modified samples. The uptake is as low as 0.115 mmol g^{-1}. Many adsorbents so far have been prepared for removal of organic sulfur compounds. For Ce(IV) exchanged Y zeolite, the adsorption capacity is 0.122 mmol g^{-1} with 297 ppmw of sulfur in commercial diesel (Hernandez-Maldonado and Yang, 2004a). The Cu(I)/SBA-15 adsorbent is derived from modification of SBA-15 with CuCl. The sulfur capacity of this adsorbent is 0.123 mmol g^{-1} with 760 ppmw of sulfur in aromatic oil (Dai et al., 2006). Metallic nickel NPs are supported on mesoporous silica for preparation of Ni/SBA-15. This adsorbent could capture 0.053 mmol g^{-1} of sulfur with diesel containing 240 ppmw of sulfur (Park et al., 2008). These results indicate that the present $36CeO_2$-ASS adsorbent is highly competitive for application in adsorptive desulfurization. Adsorption–desorption cycles for the $36CeO_2$-ASS sample were tested according to a reported method (Oliveira et al., 2009; Rodrigues et al., 2014; Vilarrasa-Garcia et al., 2011a). Figure S3 shows the results that three cycles of adsorption and desorption could be achieved by use of this reported method.

We have noticed that with the introduction of CeO_2 in SBA-15, the sulfur capacities of the CeO_2-ASS and CeO_2-TFS samples are much higher than SBA-15. There are a number of studies which indicate that Ce(IV), with the valence electronic configuration $4f^05d^06s^0$, has high positive charge and polarizability. Sulfur compounds can be adsorbed over Ce(IV) by a direct S–M interaction (Wang et al., 2009a). The IR spectrum of the $36CeO_2$-ASS sample adsorption with model fuel was recorded (Figure S4). After adsorption with model fuel, the new bands at $\sim$3000 cm^{-1} could contribute to the interaction between the $36CeO_2$-ASS sample and sulfur via the direct S–M interaction. Thus, the enhanced performances of CeO_2-ASS and CeO_2-TFS over SBA-15 can contribute to the modified CeO_2 species, which form S–M bonds with thiophene. It should be further pointed out that the CeO_2-ASS samples show better desulfurization performances than CeO_2-TFS. The aforementioned results indicate that CeO_2 NPs in the CeO_2-ASS samples have better dispersion status than in CeO_2-TFS. Taken together, these results suggest that the desulfurization performances of the samples are consistent with the dispersion status of CeO_2 NPs. In other words, high dispersion of CeO_2 NPs is in favor of better performance on desulfurization.

Conclusions

In conclusion, with the introduction of $Ce(NO_3)_2$ into ASS, high dispersion of CeO_2 NPs can be obtained (CeO_2-ASS). The particle sizes of the CeO_2 NPs are in control of 4.4–6.3 nm in the CeO_2-ASS samples, with the CeO_2 content of 12–46 wt%. The high dispersion of CeO_2 NPs can be attributed to the ASS with template P123, which provides a confined space for the dispersion of CeO_2 NPs. However, the large CeO_2 NPs (7.0 nm) are formed for the sample originated from template-free SBA-15 (CeO_2-TFS). The high dispersion of CeO_2 NPs makes the CeO_2-ASS adsorbents better perform on desulfurization than CeO_2-TFS.

Declaration of Conflicting Interests

Funding

Supplementary Material

The Supplementary material for this article is available on the Journal site.

References

Anbia M and Mohammadi K (2008) Removal of copper-phthalocyanine from aqueous solution by cationically templated MCM-41 and MCM-48 nanoporous adsorbents. *Chinese Journal of Chemistry* 26(11): 2051–2055.

Cao BC, Shen WZ and Liu YH (2008) Adsorption desulphurization of gasoline by silver loaded onto modified activated carbons. *Adsorption Science & Technology* 26(4): 225–231.

Cheng JL, Jin SL, Zhang R, et al. (2015) Enhanced adsorption selectivity of dibenzothiophene on ordered mesoporous carbon-silica nanocomposites *via* copper modification. *Microporous and Mesoporous Materials* 212: 137–145.

Cruz P, Perez Y, del Hierro I, et al. (2016) Copper, copper oxide nanoparticles and copper complexes supported on mesoporous SBA-15 as catalysts in the selective oxidation of benzyl alcohol in aqueous phase. *Microporous and Mesoporous Materials* 220: 136–147.

Dai W, Zhou YP, Li SN, et al. (2006) Thiophene capture with complex adsorbent SBA-15/Cu(I). *Industrial & Engineering Chemistry Research* 45(23): 7892–7896.

Danmaliki GI and Saleh TA (2017) Effects of bimetallic Ce/Fe nanoparticles on the desulfurization of thiophenes using activated carbon. *Chemical Engineering Journal* 307: 914–927.

Eedugurala N, Wang Z, Chaudhary U, et al. (2015) Mesoporous silica-supported amidozirconium-catalyzed carbonyl hydroboration. *Acs Catalysis* 5(12): 7399–7414.

Feng C, Li Y and Liu X (2012) Photocatalytic degradation of imidacloprid by phosphotungstic acid supported on a mesoporous Sieve MCM-41. *Chinese Journal of Chemistry* 30(1): 127–132.

Gaudin P, Dorge S, Nouali H, et al. (2016) CuO/SBA-15 materials synthesized by solid state grinding: Influence of CuO dispersion and multicycle operation on DeSO(x) performances. *Applied Catalysis B: Environmental* 181: 379–388.

Hernandez-Maldonado AJ and Yang RT (2004a) Desulfurization of diesel fuels *via* Π-complexation with nickel(II)-exchanged X- and Y-zeolites. *Industrial & Engineering Chemistry Research* 43(4): 1081–1089.

Hernández-Maldonado AJ and Yang RT (2004b) Desulfurization of diesel fuels by adsorption *via* Π-complexation with vapor-phase exchanged Cu(I)−Y zeolites. *Journal of the American Chemical Society* 126(4): 992–993.

Jiang WJ, Yin Y, Liu XQ, et al. (2013) Fabrication of supported cuprous sites at low temperatures: An efficient, controllable strategy using vapor-induced reduction. *Journal of the American Chemical Society* 135(22): 8137–8140.

Kannan MV and Kumar GG (2016) Current status, key challenges and its solutions in the design and development of graphene based Orr catalysts for the microbial fuel cell applications. *Biosensors and Bioelectronics* 77: 1208–1220.

Khan NA, Kim CM and Jhung SH (2017) Adsorptive desulfurization using Cu-Ce/metal-organic framework: Improved performance based on synergy between Cu and Ce. *Chemical Engineering Journal* 311: 20–27.

Li Y, Wang XX and Song CS (2016) Spectroscopic characterization and catalytic activity of Rh supported on CeO$_2$-modified Al$_2$O$_3$ for low-temperature steam reforming of propane. *Catalysis Today* 263: 22–34.

Liu XY, Tian BZ, Yu CZ, et al. (2002) Room-temperature synthesis in acidic media of large-pore three-dimensional bicontinuous mesoporous silica with *Ia3d* symmetry. *Angewandte Chemie International Edition* 41(20): 3876–3878.

Moghadam FR, Azizian S, Bayat M, et al. (2017) Extractive desulfurization of liquid fuel by using a green, neutral and task specific phosphonium ionic liquid with glyceryl moiety: A joint experimental and computational study. *Fuel* 208: 214–222.

Oliveira MLM, Miranda AAL, Barbosa C, et al. (2009) Adsorption of thiophene and toluene on NaY zeolites exchanged with Ag(I), Ni(II) and Zn(II). *Fuel* 88(10): 1885–1892.

Park JG, Ko CH, Yi KB, et al. (2008) Reactive Adsorption of sulfur compounds in diesel on nickel supported on mesoporous silica. *Applied Catalysis B: Environmental* 81(3–4): 244–250.

Rodrigues AKO, Ramos JET, Cavalcante CL, et al. (2014) Pd-loaded mesoporous silica as a robust adsorbent in adsorption/desorption desulfurization cycles. *Fuel* 126: 96–103.

Shang H-Y, Liu C-G, Zhao R-Y, et al. (2004) XPS characterization of carbon nanotube supported CoMo hydrodesulfurization catalysts. *Chinese Journal of Chemistry* 22(11): 1250–1256.

Shao XC, Zhang XT, Yu WG, et al. (2012) Effects of surface acidities of MCM–41 modified with MoO$_3$ on adsorptive desulfurization of gasoline. *Applied Surface Science* 263: 1–7.

Shi CW, Wu YF, Chen WY, et al. (2017) Synthesis and characteristics of Ce modified HY/SBA-15 and its desulfurization performance for simulated oil. *Journal of Porous Materials* 24(2): 381–388.

Singh R and Kunzru D (2016) Hydrodesulfurization of dibenzothiophene on NiMo/γ-Al$_2$O$_3$ washcoated monoliths. *Fuel* 163: 180–188.

Sitamraju S, Xiao J, Janik MJ, et al. (2015) Active sites on Ti-Ce mixed metal oxides for reactive adsorption of thiophene and its derivatives: A DFT study. *Journal of Physical Chemistry C* 119(11): 5903–5913.

Song H, Chang YX and Song HL (2016) Deep adsorptive desulfurization over Cu, Ce bimetal ion-exchanged Y-typed molecule sieve. *Adsorption – Journal of the International Adsorption Society* 22(2): 139–150.

Song H, Cui X, Song H, et al. (2014) Characteristic and adsorption desulfurization performance of Ag-Ce bimetal ion-exchanged Y zeolite. *Industrial & Engineering Chemistry Research* 53(37): 14552–14557.

Song H, Wan X, Dai M, et al. (2013) Deep desulfurization of model gasoline by selective adsorption over Cu-Ce bimetal ion-exchanged Y zeolite. *Fuel Processing Technology* 116: 52–62.

Song X, Sun L, He G, et al. (2011) Isolated Cu(I) sites supported on β-cyclodextrin: An efficient Π-complexation adsorbent for thiophene capture. *Chemical Communications* 47(2): 650–652.

Speder J, Zana A and Arenz M (2016) The colloidal tool-box approach for fuel cell catalysts: Systematic study of perfluorosulfonate-ionomer impregnation and Pt loading. *Catalysis Today* 262: 82–89.

Stein A (2003) Advances in microporous and mesoporous solids. *Advanced Materials* 15(10): 763–775.

Sun LB, Liu XQ and Zhou HC (2015) Design and fabrication of mesoporous heterogeneous basic catalysts. *Chemical Society Reviews* 44(15): 5092–5147.

Sun YY and Prins R (2008) Hydrodesulfurization of 4,6-dimethyldibenzothiophene over noble metals supported on mesoporous zeolites. *Angewandte Chemie International Edition* 47(44): 8478–8481.

Thomas A (2010) Functional materials: From hard to soft porous frameworks. *Angewandte Chemie International Edition* 49(45): 8328–8344.

Tian BZ, Liu XY, Yu CZ, et al. (2002) Microwave assisted template removal of siliceous porous materials. *Chemical Communications* 38(11): 1186–1187.

Tian WH, Sun LB, Song XL, et al. (2010) Adsorptive desulfurization by copper species within confined space. *Langmuir* 26(22): 17398–17404.

Vilarrasa-Garcia E, Azevedo DCS, Braos-Garcia P, et al. (2011a) Synthesis and characterization of metal-supported mesoporous silicas applied to the adsorption of benzothiophene. *Adsorption Science & Technology* 29(7): 691–704.

Vilarrasa-Garcia E, Azevedo DCS, Braos-Garcia P, et al. (2011b) Synthesis and characterization of metal-supported mesoporous silicas applied to the adsorption of benzothiophene. *Adsorption Science and Technology* 29(7): 691–704.

Vit Z, Gulkova D, Kaluza L, et al. (2015) Pd-Pt catalysts on mesoporous SiO_2-Al_2O_3 with superior activity for HDS of 4,6-dimethyldibenzothiophene: Effect of metal loading and support composition. *Applied Catalysis B: Environmental* 179: 44–53.

Wang J, Xu F, Xie WJ, et al. (2009a) The enhanced adsorption of dibenzothiophene onto cerium/nickel-exchanged zeolite Y. *Journal of Hazardous Materials* 163(2–3): 538–543.

Wang LF, Sun BD, Yang FH, et al. (2012) Effects of aromatics on desulfurization of liquid fuel by Π-complexation and carbon adsorbents. *Chemical Engineering Science* 73: 208–217.

Wang YH, Yang FH, Yang RT, et al. (2006) Desulfurization of high-sulfur jet fuel by Π-complexation with copper and palladium halide sorbents. *Industrial and Engineering Chemistry Research* 45(22): 7649–7655.

Wang YH, Yang RT and Heinzel JM (2009b) Desulfurization of jet fuel JP-5 light fraction by MCM-41 and SBA-15 supported cuprous oxide for fuel cell applications. *Industrial and Engineering Chemistry Research* 48(1): 142–147.

Xiao J, Wang XX, Chen YS, et al. (2013a) Ultra-deep adsorptive desulfurization of light-irradiated diesel fuel over supported TiO_2-CeO_2 adsorbents. *Industrial and Engineering Chemistry Research* 52(45): 15746–15755.

Xiao J, Wang XX, Fujii M, et al. (2013b) A novel approach for ultra-deep adsorptive desulfurization of diesel fuel over TiO_2-CeO_2/MCM-48 under ambient conditions. *AIChE Journal* 59(5): 1441–1445.

Xiong L, Yan XM and Mei P (2010) Synthesis and characterization of a ZrO_2/AC composite as a novel adsorbent for dibenzothiophene. *Adsorption Science & Technology* 28(4): 341–350.

Xu H, Zhang DD, Wu FM, et al. (2017) Deep oxidative desulfurization of fuels based on C(4)mimCl $CoCl_2$ ionic liquid oxone solutions at room temperature. *Fuel* 208: 508–513.

Yang RT, Hernández-Maldonado AJ and Yang FH (2003) Desulfurization of transportation fuels with zeolites under ambient conditions. *Science* 301(5629): 79–81.

Yin Y, Jiang WJ, Liu XQ, et al. (2012) Dispersion of copper species in a confined space and their application in thiophene capture. *Journal of Materials Chemistry* 22(35): 18514–18521.

Yin Y, Tan P, Liu XQ, et al. (2014) Constructing a confined space in silica nanopores: An ideal platform for the formation and dispersion of cuprous sites. *Journal of Materials Chemistry A* 2(10): 3399–3406.

Yin Y, Zhu J, Liu XQ, et al. (2016) Simultaneous fabrication of bifunctional Cu(I)/Ce(IV) sites in silica nanopores using a guests-redox strategy. *RSC Advances* 6(74): 70446–70451.

Yue MB, Sun LB, Cao Y, et al. (2008) Efficient CO_2 capturer derived from as-synthesized MCM-41 modified with amine. *Chemistry A European Journal* 14(11): 3442–3451.

Zhang F, Chai Q and Li H-X (2008) CO_2-promoted water-medium Ullmann reaction over a Pd/phenyl-SBA-15 mesoporous catalyst. *Chinese Journal of Chemistry* 26(1): 25–29.

Zhao DY, Feng JL, Huo QS, et al. (1998) Triblock copolymer syntheses of mesoporous silica with periodic 50 to 300 angstrom pores. *Science* 279(5350): 548–552.

Supplementary Information

Functionalization of SBA-15 with CeO₂ Nanoparticles for Adsorptive Desulfurization: Matters of Template P123

Yu Yin*[,a], Zhi-Hao Wen [a], Xiao-Qin Liu [b], Ai-Hua Yuan [a], and Lei Shi [c]

[a] School of Environmental and Chemical Engineering, Jiangsu University of Science and Technology, Zhenjiang 212003, P. R. China

[b] State Key Laboratory of Materials-Oriented Chemical Engineering, College of Chemistry and Chemical Engineering, Nanjing Tech University, Nanjing 210009, P. R. China

[c] State Key Laboratory of Lake Science and Environment, Nanjing Institute of Geography and Limnology, Chinese Academy of Sciences, Nanjing 210008, P. R. China

Supplementary Experimental Details

Materials Characterization

TEM images were recorded on a JEM-200CX electron microscope operated at 200 kV. X-ray photoelectron spectroscopy (XPS) analysis was conducted on a Physical Electronic PHI-550 spectrometer equipped with an Al Kα X-ray source (hv = 1486.6 eV) and was operated at 10 kV and 35 mA. Elemental analysis experiment was carried on Elementar Vario EL III instrument. Fourier transform infrared (IR) spectra were recorded on a Nicolet Nexus 470 spectrometer with a spectra resolution of 2 cm⁻¹ using transparent KBr pellets. For the measurement of IR spectrum after adsorption with model fuel, the sample was added to the model fuel and stirred for more than four hours. After drying, the IR spectrum were recorded.

Adsorption-desorption Experiment

The adsorption-desorption cycles were investigated. Simulated fuel (550 ppm w) was pumped into the adsorbent with a mini creep pump at a rate of 3.0 mL·h⁻¹ until near saturation. Then the feed was switched to pure isooctane in order to regeneration the column. When the effluent sulfur concentration descended to near zero, the feed was again switched to simulated fuel. Three desulfurization/regeneration cycles were performed.
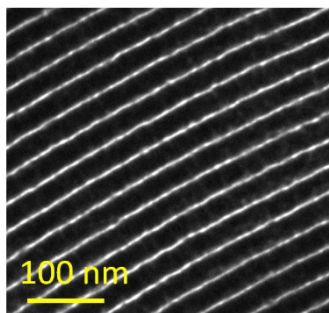
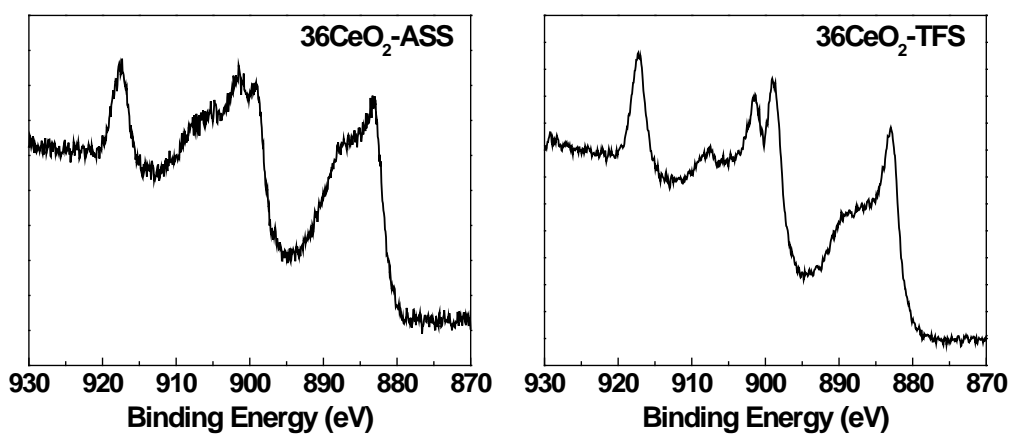# Supplementary Figures

Figure S1. TEM image of SBA-15.

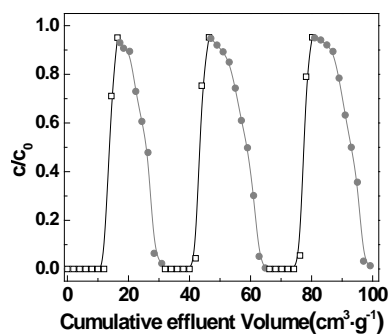**Figure S2** XPS peak fitting of Ce 3d spectra of the samples.

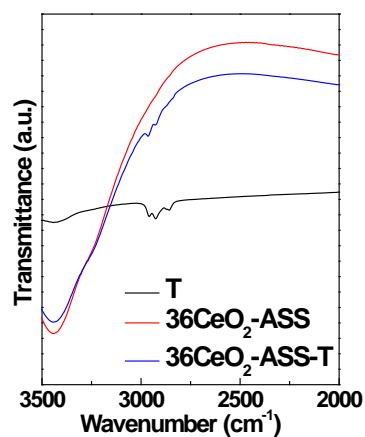**Figure S3.** Adsorption-desorption cycles in a fixed-bed adsorber with the $36CeO_2$-ASS sample.

Figure S4. IR spectra of the 36CeO$_2$-ASS sample before and after adsorption with model fuel

Table S1 Atomic concentration of elements in the 36CeO$_2$-ASS and 36CeO$_2$-TFS samples

Sample	Si	O	Ce
Theoretical content	2.56	66.67	30.78
36CeO$_2$-ASS	25.69	68.56	1.03
36CeO$_2$-TFS	24.85	69.85	1.12

Table S2 Elemental analysis results of C and H weight ratio in the samples

sample	C (wt %)	H (wt %)
as synthesized SBA-15	30.59	5.83
SBA-15	0.32	2.79
36CeO$_2$-ASS	0.10	2.03
36CeO$_2$-TFS	0.11	1.64

3